TU Delft

Delft University of Technology

Quantifying the Precision of Single-Molecule Torque and Twist Measurements Using Allan Variance

van Oene, Maarten M.; Ha, Seungkyu; Jager, Tessa; Lee, Mina; Pedaci, Francesco; Lipfert, Jan; Dekker, Nynke H.

DOI
10.1016/j.bpj.2018.02.039

Publication date
2018

Document Version
Accepted author manuscript

Published in
Biophysical Journal

Citation (APA)
van Oene, M. M., Ha, S., Jager, T., Lee, M., Pedaci, F., Lipfert, J., & Dekker, N. H. (2018). Quantifying the Precision of Single-Molecule Torque and Twist Measurements Using Allan Variance. *Biophysical Journal*, *114*(8), 1970-1979. https://doi.org/10.1016/j.bpj.2018.02.039

Important note
To cite this publication, please use the final published version (if applicable).
Please check the document version above.

Copyright
Other than for strictly personal use, it is not permitted to download, forward or distribute the text or part of it, without the consent of the author(s) and/or copyright holder(s), unless the work is under an open content license such as Creative Commons.

Takedown policy
Please contact us and provide details if you believe this document breaches copyrights.
We will remove access to the work immediately and investigate your claim.

This work is downloaded from Delft University of Technology.
For technical reasons the number of authors shown on this cover page is limited to a maximum of 10.

Quantifying the Precision of Single-Molecule Torque and Twist Measurements using Allan Variance

Running Title: Quantifying Torque and Twist Precision

Maarten M. van Oene[1,†], Seungkyu Ha[1,†], Tessa Jager[1], Mina Lee[1], Francesco Pedaci[1], Jan Lipfert[1,2,*], and Nynke H. Dekker[1,*]

[1]Department of Bionanoscience, Kavli Institute of Nanoscience, Delft University of Technology, Delft, the Netherlands
[2]Department of Physics, Nanosystems Initiative Munich, and Center for Nanoscience, LMU Munich, Munich, Germany

†Maarten M. van Oene and Seungkyu Ha contributed equally to this work.
*Correspondence: jan.lipfert@lmu.de or n.h.dekker@tudelft.nl

Mina Lee's present address is Center for Nano-Bio Measurement, Korea Research Institute of Standards and Science, Daejeon, Korea
Francesco Pedaci's present address is Department of Single-Molecule Biophysics, Centre de Biochimie Structurale, CNRS UMR 5048 UM INSERM U 1054, Montpellier, France

Keywords: Torque, Measurement Precision, Allan Variance, Magnetic Tweezers, Optical Tweezers, Single-Molecule Techniques

© 2018 Manuscript version made available under CC-BY-NC-ND 4.0 license https://creativecommons.org/licenses/by-nc-nd/4.0/

Abstract

Single-molecule manipulation techniques have provided unprecedented insights into the structure, function, interactions, and mechanical properties of biological macromolecules. Recently, the single-molecule toolbox has been expanded by techniques that enable measurements of rotation and torque, such as the optical torque wrench and several different implementations of magnetic (torque) tweezers. While systematic analyses of the position and force precision of single-molecule techniques have attracted considerable attention, their angle and torque precision have been treated in much less detail. Here, we propose the Allan deviation as a tool to systematically quantitate angle and torque precision in single-molecule measurements. We apply the Allan variance method to experimental data from our implementations of (electro-) magnetic torque tweezers and an optical torque wrench and find that both approaches can achieve a torque precision better than 1 pN·nm. The optical torque wrench, capable of measuring torque on (sub)-millisecond timescales, provides the best torque precision for measurement times $\lesssim$ 10 s, after which drift becomes a limiting factor. For longer measurement times, the magnetic torque tweezers with their superior stability provide the best torque precision. Use of the Allan deviation enables critical assessments of the torque precision as a function of measurement time across different measurement modalities, and provides a tool to optimize measurement protocols for a given instrument and application.

Introduction

Single-molecule manipulation techniques have provided unprecedented insights into the structure, function, interactions, and mechanical properties of biological macromolecules (1-7). Many single-molecule manipulation techniques, notably optical tweezers and atomic force microscopy, naturally operate in the space of (linear) extension and force. However, frequently biological macromolecules are subject to torsional strain, and the molecular motors that translocate along them must be able to progress amidst accumulated twist and torque. To quantify these phenomena, a number of techniques that enable measurements of rotation angle and torque (8, 9) have been developed recently. Examples of such techniques (reviewed in Ref. (9)) include the rotor bead tracking assay (10-15), optical torque tweezers (16-28), and various extensions of magnetic tweezers, comprising magnetic torque tweezers (29-32), freely-orbiting magnetic tweezers (33, 34), and electromagnetic torque tweezers (35). While the field of force spectroscopy has benefited from systematic analyses of the position and force precision of single-molecule techniques (36-44), torque and twist measuring techniques would be enriched by a better understanding of the achievable precision in angular detection and the determination of torque.

Here, we propose the Allan deviation (AD) (38-49) as a criterion to systematically quantitate the angle and torque precision in single-molecule measurements. The AD allows us to critically assess the torque precision as a function of measurement time across different measurement modalities (e.g. magnetic versus optical torque tweezers) that rely on distinct physical principles. Being a real space quantity and having the same units as the observable of interest, it provides an intuitive and direct way to quantify and interpret precision (38-44). In addition to enabling direct quantitative comparisons of different torque and twist measurement strategies, use of the AD in a systematic way provides an experimental user with a very convenient tool with which to optimize the measurement protocol for a given instrument and system. Here, we investigate the AD method using simulated traces and demonstrate its application to various implementations of (electro-) magnetic torque tweezers (eMTT and MTT) and an optical torque wrench (OTW). Using the AD analysis, we arrive at clear recommendations, e.g. for the optimal in-plane magnetic field strength in the eMTT and for choosing an optimal trapping laser power in the OTW.

Materials and Methods

Definition and properties of the Allan deviation. Given a time series of N observations of some quantity θ, recorded at a sampling frequency f_s over a total measurement time $t_{meas} = N/f_s$, the Allan variance (AV) of θ for the time interval τ is defined as (42, 43, 45):

$$\sigma_\theta^2(\tau) = \frac{1}{2}\langle(\bar{\theta}_{i+1} - \bar{\theta}_i)^2\rangle, \qquad \textbf{Equation 1}$$

where $\bar{\theta}_i$ is the mean of the i^{th} measurement interval of length τ. The angle bracket <…> denotes the arithmetic mean over all measurement intervals. In other words, the AV is one half of the averaged square distance between the means of neighboring intervals. From its definition, the value of the AV is always greater than zero; it can only be computed for time intervals $\tau \leq t_{meas}/2$; it is additive for independent signals, i.e., the AV is the sum of the individual AVs; and it is linear, i.e., a linear scaling of θ, $\theta' = \alpha \cdot \theta$, will simply scale the AV: $\sigma_{\theta'}{}^2(\tau) = \alpha^2 \cdot \sigma_\theta^2(\tau)$. The property of linearity is convenient since it allows for analysis of uncalibrated signals with the AV (e.g. one can analyze the voltage signal from a quadrant photodiode, position sensing detector, or photodiode without having to first convert to position or torque units). In addition, the linearity enables simple conversion from angle to torque signal (by multiplication with the rotational trap stiffness, κ_θ, in units of pN·nm/rad) before or after evaluation of the AV. The Allan deviation is defined as the square root of the Allan variance: $\sigma_\theta(\tau) = (\sigma_\theta^2)^{1/2}$. Since Allan deviation has the same units as the quantity under investigation, it may be more intuitive to report Allan deviations rather than Allan variances.

Computation of the Allan variance. In practice, the AV is estimated from a data set with a finite number of measurements using a discrete form of **Eq. 1**. In the simple form of the AV, the data is split in M bins of m data points each, and the value of each bin is the mean over its m data points. The mean-squared difference of consecutive bins estimates the AV:

$$\sigma_\theta^2(m\tau_s) = \frac{1}{2(M-1)} \sum_{i=1}^{M-1} (\bar{\theta}_{i+1} - \bar{\theta}_i)^2, \qquad \textbf{Equation 2}$$

where τ_s is the sampling period and $\bar{\theta}_i$ is the mean of the i^{th} bin of length $m\tau_s$. The sampling period is taken to equal the integration time. For camera-based detection in the magnetic tweezers this assumes no dead time between frames, which is justified given the typical dead time (~10 μs) relative to the integration time (~10 ms). For photodiode-based

detection in the OTW, the situation is quite different: while the effective integration time is very fast (~10 ns), the photodiode is only read out at ~100 kHz. The inverse of this rate (~10 μs) is analogous to a dead time, as no signal averaging occurs. Thus, in the OTW the dead time far exceeds the integration time. However, the application of **Eq. 2** remains valid in all situations considered in this work since the sampling period is much shorter than the characteristic time of the system (**Supplementary Text S1**). For each value of m, m frameshifts exist to compute the AV (**Fig. 1A**). The use of all of these frameshifts improves the estimate of the AV, and is known as the "overlapping" AV (**Eq. S3** in **Supplementary Text S2**).

While the AV is defined for all values of m (up to the maximum $m = N/2$), the AVs for successive values of m are not independent and can be nearly identical, because most values in a bin of size m are identical to the values in a bin of size $m + 1$. For fitting of the AV data, it is therefore advantageous to calculate the octave-sampled AV by choosing $m = 2^{\text{integer}}$, which ensures nearly independent differences (46, 47). We compute the AV (39) using a publicly available Matlab function (49). All AV curves are fit using maximum likelihood estimation (MLE) using the shape factor by Lansdorp and Saleh (47) (**Eq. S4** in **Supplementary Text S3**).

Analytic expression for the Allan variance of a Brownian particle in a harmonic trap. We employ the analytical expression given by Lansdorp and Saleh (47, 48) for the AV of a particle undergoing Brownian motion in a harmonic well, and apply it to the case of rotational motion:

$$\sigma_\theta^2 = A\left(\frac{\tau_c}{\tau}\right)^2\left(2\frac{\tau}{\tau_c} + 4\exp\left(-\frac{\tau}{\tau_c}\right) - \exp\left(-2\frac{\tau}{\tau_c}\right) - 3\right), \qquad \textbf{Equation 3}$$

where $A = k_BT/\kappa_\theta$ and $\tau_c = \gamma_\theta/\kappa_\theta$. Here, γ_θ is the rotational friction coefficient and κ_θ is the trap stiffness of the rotational trap. Note that $k_BT/\kappa_\theta = Var(\theta)$ according to the equipartition theorem. We determine the friction coefficient γ_θ and the trap stiffness κ_θ by fitting the expression (**Eq. 3**) to our data using a maximum likelihood estimation algorithm (47). In the short time averaging limit, where diffusion is dominant, the AV reduces to:

$$\sigma_\theta^2 = \frac{2}{3}D\tau, \qquad \textbf{Equation 4}$$

where D is the diffusion constant, which, according to the Einstein–Smoluchowski relation, equals $k_B T/\gamma_\theta$.

In most single-molecule experiments, the short time regime provides little information about the system under study, because the particle can barely respond to changes on these time scales, particularly for often relatively slow torque measurements. For long averaging times, the AV reaches the so-called thermal limit, where it reduces to:

$$\sigma_\theta^2 = 2\,A\frac{\tau_c}{\tau} = 2\frac{Var(\theta)}{n} = \frac{2k_B T\gamma_\theta}{\kappa_\theta^2 \tau}, \qquad \textbf{Equation 5}$$

where $n = \tau/\tau_c$ defines the number of independent observations. The averaging reduces the variance with the number of independent measurements n and, therefore, the AV decreases inversely proportional to τ, improving the angle precision. In between these two limits, the AV peaks at τ_{max}, with the best estimate of τ_{max} (= $1.8926\tau_c$) coming from the numerical solution of **Eq. 3** as opposed to the analytical solution of **Eqs. 4, 5** (= $\sqrt{3}\tau_c$).

Eqs. 3-5 can be converted from angle to torque AV by straightforward application of the property of linearity: in the harmonic approximation, torque Γ is proportional to angle θ ($\Gamma = -\kappa_\theta \cdot \theta$), and hence $\sigma_\Gamma^2 = \kappa_\theta^2 \cdot \sigma_\theta^2$. Thus, the thermal limit of the torque AV is given by:

$$\sigma_\Gamma^2 = \frac{2k_B T\gamma_\theta}{\tau}. \qquad \textbf{Equation 6}$$

In this limit, the AV for torque is independent of the trap stiffness κ_θ, suggesting that stiffness has no effect on the torque precision in the regime where the measurement precision is limited by thermal fluctuations (32).

Stochastic simulations of rotational motion. To test our Allan deviation analysis and to illustrate the effects of various system parameters, we simulate stochastic time traces of rotational motion using numerical solutions to the corresponding overdamped Langevin equation (**Fig. 1**). To simulate the rotation angle as a function of time $\theta(t)$, we discretize time into time steps Δt. The angle at time step $i + 1$, θ_{i+1}, is given by the discretized overdamped Langevin equation as:

$$\theta_{i+1} = \theta_i + \left(\frac{\Gamma_{external} + \Gamma_{thermal}}{\gamma_\theta}\right)\Delta t, \qquad \textbf{Equation 7}$$

where the right-hand side only involves quantities known at time step i; γ_θ is the rotational friction coefficient (in units of pN·nm·s), $\Gamma_{external}$ is the external torque, and

$\Gamma_{thermal} = N(0,1)\cdot(2k_BT\gamma_\theta/\Delta t)^{1/2}$, with the thermal energy, $k_BT \approx 4.1$ pN·nm at room temperature, and $N(0,1)$ is Gaussian distributed noise with zero mean and unit standard deviation. The Langevin dynamics simulations were implemented using custom Matlab routines (**Supplementary Text S4**).

Allan deviation measurements with magnetic tweezers. Torque application in magnetic tweezers relies on the alignment of superparamagnetic micron-sized beads or microspheres (referred to as 'beads' from here on after) with an externally applied magnetic field (5, 29, 50). Both MTT and eMTT employ a predominantly vertically oriented field generated by a cylindrical magnet, and a smaller field in the horizontal direction generated by a side magnet in the MTT (32) (**Fig. 2A**) or by electromagnets in the eMTT (35) (**Fig. 3A**). The in-plane field generates a sufficiently weak angular trap to perform experiments on soft molecules, like DNA. Torque measurements in MTT and eMTT rely on tracking the rotational angle of the bead and observing changes in the equilibrium angle position of the bead inside the trap upon applying twist to a molecule of interest tethered between a surface and the magnetic bead. The torque is determined from the product of the angular shift and the trap stiffness, and hence the angle Allan deviation can be determined directly from the angular traces, while the torque Allan deviation requires a calibrated trap stiffness. Limitations in angular tracking will therefore also affect the torque precision.

Our MTT and eMTT measurements of the Allan deviation use custom-built instruments described in detail elsewhere (32, 35). In brief, they employ double-stranded DNA constructs bound to a flow cell surface via multiple digoxigenin-antidigoxigenin interactions and to superparamagnetic beads via multiple biotin-streptavidin interactions in PBS buffer. Bead sizes and DNA tether lengths are indicated in the main text and figure legends.

Allan deviation measurements with optical tweezers. The OTW is an extension of conventional optical tweezers that exploits the exchange of angular momentum between a nanofabricated, birefringent particle and a polarized trapping beam to apply and measure torque (16-28). Unlike the magnetic tweezers, which employ standard commercially available magnetic beads (whose magnetic anisotropy governs the

achievable torque levels (50), and where a choice of diameters permits control over the drag coefficient), for the OTW no comparable particles exist. Instead, one typically custom fabricates birefringent dielectric particles using one of several fabrication routes (top-down, bottom-up), materials (quartz SiO_2 (0.009), vaterite $CaCO_3$ (0.1), calcite $CaCO_3$ (-0.16), rutile TiO_2 (0.26); optical birefringences specified in parentheses), shapes (spherical, cylindrical, etc.), and dimensions (with a size scale of a few μm being most prevalent) (23-28). In our custom-built instrument (22), we measure on cylindrically shaped rutile TiO_2 nanoparticles (diameter ~215 nm, height ~765 nm) fabricated in our cleanroom facility (26).

In the OTW, the optical tweezers trap a birefringent cylinder with its long axis aligned with the propagation direction of the light (**Fig. 4A**). The linear polarization of the trapping laser clamps the angular position of the rutile TiO_2 cylinder, and rotation of this polarization controls rotation of the particle about its long axis (26). The imbalance between left and right circularly polarized components in the output of the trap provides a direct measure for the exchange of angular momentum inside the trap, and hence a measure for the optical torque transferred to the particle. In the Allan deviation measurements, we fixed the direction of the linear polarization, and measured the fluctuations around this equilibrium position (**Supplementary Figs. S8A, S9A**). The power of the trapping laser is tuned using a half-wave plate and a polarizing beam splitter, in the range of 10–80 mW at the laser focus.

Results

The Allan deviation (AD) is the square root of the Allan variance, a type of variance that uses samples averaged over variable time intervals τ and that is computed from the difference between neighboring intervals (**Materials and Methods**). While other approaches to quantify precision exist (e.g., other variances, autocorrelation, or power spectrum analyses (**Supplementary Text S5**, **S6**)), we find AD to be a particularly convenient measure for several reasons: i) the AD at time τ provides a direct and intuitive measure of the precision expected for a measurement of a given duration; ii) being a real space quantity, the AD is immediately in the same units as the measured quantity of interest; iii) the AD is powerful in detecting low frequency, long time scale drifts (43), which are critical for single-molecule measurements of torque and twist; and iv) the AD

can be straightforwardly computed from the raw experimental data, without the need to be calibrated *a priori*. In the following, we explore the use of AD to quantify the angle and torque precision of single-molecule measurements. First, we present the results of stochastic simulations to introduce the concept of AD and validate our approach. We then use AD to compare the precision of three different single-molecule torque spectroscopy techniques: magnetic torque tweezers (MTT), electromagnetic torque tweezers (eMTT), and an optical torque wrench (OTW).

Allan deviation analysis of simulated traces. To explore the effects of the various system parameters on the AD, we simulated traces of the stochastic rotational motion of a bead subject to Brownian fluctuations while held in a harmonic trap (**Fig. 1B-D** and **Supplementary Fig. S1**). The simulated rotational motion (about an axis through the bead's center of mass) reveals the effects of varying rotational trap stiffness κ_θ and rotational drag coefficient γ_θ on the angular time trace (**Fig. 1B**) and on the angle AD (**Fig. 1C**) and torque AD (**Fig. 1D**). In the green data set, γ_θ = 10 pN·nm·s and κ_θ = 1000 pN·nm/rad, such that the characteristic time is $\tau_c = \gamma_\theta/\kappa_\theta$ = 10 ms. To compare the effect of different drag coefficients, we simulate the red data set with the same stiffness but a ten-fold higher drag coefficient, γ_θ = 100 pN·nm·s. To compare the effect of different stiffnesses, we generate the blue data set with the same drag coefficient as the green data set but ten-fold lower trap stiffness, κ_θ = 100 pN·nm/rad. All other parameters are identical for the three simulated traces.

The simulated angle traces provide an instructive example of how the system parameters affect the observed behavior. The widths of the histograms (**Fig. 1B**) – and thus the amplitude of the angular fluctuations – are indifferent to changes in drag coefficient (compare green and red datasets), but are affected by changes in stiffness (compare green and blue datasets); a decrease in stiffness causes increased angular fluctuations, as expected from the equipartition theorem. Another feature visible in the angle traces is the time scale over which the angular fluctuations occur. The fluctuations in the green data appear "denser" on the time axis, compared to the red and blue data, due to the fact that the characteristic time τ_c for the green dataset (10 ms) is smaller than for the red and blue datasets (100 ms).

The ADs (**Fig. 1C**,**D**) for our simulated traces all display the expected trend of an initial rise proportional to $\tau^{1/2}$ and a transition to a decrease proportional to $\tau^{-1/2}$ for larger τ (43). Changing the drag coefficient causes a shift of the curve on the time axis in both angle and torque Allan deviations (green and red datasets). This shift indicates that a higher drag coefficient is linked to slower dynamics, consistent with the higher characteristic time τ_c. For the angle AD (**Fig. 1C**), the change in stiffness initially has no effect: the curves overlap in the diffusion limit (green and blue datasets, **Eq. 4**). However, at longer time scales, a higher stiffness results in an improved angular precision (**Eq. 5**). In contrast, different stiffnesses do not alter the torque precision for large τ (**Fig. 1D**), since in the thermal limit, the torque precision is independent of the trap stiffness κ_θ (**Eq. 6**). The analytical expression for the Allan variance (**Eq. 3**) provides an excellent fit to the data, and we recover the values for κ_θ and γ_θ input into the simulations, confirming the validity of the method (**Fig. 1C**,**D**, where the range of fitted data, indicated by the black solid lines, is constrained at the shortest and longest integration time limits to avoid the influence of noise not taken into consideration in **Eq.3**).

Angle and torque precision in the MTT. The MTT employ a cylindrical magnet to generate a predominantly vertically oriented field and a side magnet to apply an additional, smaller field in the horizontal direction. MTT measure torque by detecting changes in the equilibrium position of the bead-rotation angle about the tether axis upon over- and underwinding nucleic acid tethers (30-32) (**Materials and Methods** and **Supplementary Fig. S2A-C**). Here, we analyze traces of angular fluctuations recorded in our MTT implementation (**Fig. 2A**) using a 2.8 μm diameter magnetic bead and a 1 μm diameter non-magnetic fiducial marker bead to track the rotation angle about the tether axis from analysis of the camera images (51) (**Fig. 2A**, inset). We focus on a representative data set consisting of 32 angle traces, recorded while over- and underwinding a 7.9 kbp DNA molecule tethered between the magnetic bead and the flow cell surface and held at a stretching force of ~2 pN (**Supplementary Fig. S2C**). Upon over- and underwinding the DNA by integer numbers of turns, systematic changes of the equilibrium angle position are visible (**Supplementary Fig. S2C**, middle panel, left axis). These can be related to the changes in the torque exerted by the molecule (**Supplementary Fig. S2C**, middle panel, right axis) by multiplying with the mean trap stiffness (deduced from the fits to AD curves, as detailed below; and equivalent to deducing the trap stiffness from the standard

deviation of the angular fluctuations, **Supplementary Fig. S2C**, top panel). In addition, we observe that tether extension decreases rapidly past the buckling point of the DNA molecule for positive turns (corresponding to overwinding), but stays approximately constant for negative turns (corresponding to underwinding), due to torque-induced DNA melting (32, 52) (**Supplementary Fig. S2C**, bottom panel).

Applying our AD analysis to the angle traces recorded in the MTT at different numbers of applied turns reveals some variability, but indicates that we generally reach an angle precision of ~1° for a 50 s measurement (**Fig. 2B**). From fits of the analytical expression (**Eq. 3**) to the angle AV data, we obtain the trap stiffness for each trace (**Fig. 2D**), revealing a ~13% variation from trace to trace, without any systematic changes throughout the measurement (**Supplementary Fig. S2D**). This yields a mean trap stiffness of 339 ± 45 pN·nm/rad, in excellent agreement with the value obtained from directly computing the standard deviation of the angular fluctuations (330 ± 46 pN·nm/rad). Multiplying each angle AD curve by its fitted value of the trap stiffness, we convert the angle to a torque signal (**Fig. 2C**). AD analysis of the torque signal indicates that the torque precision in the MTT follows the thermal limit (**Fig. 2C**, dashed magenta line) for measurement times longer than ~2 s and reaches ~5 pN·nm after 50 s (**Fig. 2C**). These results are consistent with our previous torque precision estimate for this setup (32) of 1–3 pN·nm for a 300 s measurement. In addition, we obtain values for the drag coefficient from the AV fits that exhibit systematic changes with DNA tether extensions, increasing by ~70–80% upon decreasing the extension from 2.4 μm to 0.7 μm (**Fig. 2E**). Both the observed value for the drag coefficients and the dependence on DNA extension are in reasonable agreement with the predictions of a model (**Fig. 2E**, solid black line) that describes the rotation of a 2.8 μm diameter bead along a circular trajectory, taking into account the increase in friction coefficient due to the proximity of the flow cell surface (53, 54) (see **Eq. S10** in **Supplementary Text S7**). The observed dependence of the friction coefficient on DNA tether extension highlights the ability of our AD analysis to detect subtle changes in measurement parameters and demonstrates the importance of taking into account surface proximity effects when evaluating friction coefficients in single-molecule measurements (55).

Angle and torque precision in the eMTT at different fields. eMTT (**Fig. 3A**) are similar to MTT, with the main difference that in the eMTT electromagnets (implemented as two pairs of Helmholtz coils) generate the field in the horizontal direction. eMTT have the advantage over MTT that the horizontal field component is readily tunable by altering the current in the Helmholtz coils (35). The ability to tune the trap stiffness, however, raises the question what stiffness, if any, is optimal for a given torque measurement application. To explore the effects of trap stiffness and bead size, we measured angular fluctuations and analyzed the ADs of several, differently-sized, DNA-tethered beads in the eMTT (**Supplementary Figs. S3-S5**); for each bead size, measurements were carried out at different applied currents in the Helmholtz coils, corresponding to different applied fields in the horizontal direction. We present the results of a single 0.7 μm diameter bead trapped at different magnetic field strengths in **Fig. 3**.

From the AD of the angle signal in the eMTT, it is apparent that higher fields, corresponding to higher trap stiffnesses, give rise to a better angle precision (**Fig. 3B**). For the 0.7 μm diameter beads, the measurements reach ~1° precision in 3 s at the highest field strength of 16 mT (**Fig. 3B**, lightest brown). This is much faster than what was observed in the MTT (~50 s, **Fig. 2B**), despite the lower trap stiffness employed in the eMTT, and results from our use of much smaller beads in the eMTT measurement. Converting the angle AD to torque AD by multiplication with the trap stiffness (itself deduced by fitting the corresponding angle AD curve), we find that the torque precision measurements are independent of trap stiffness in the thermal limit, i.e. at times longer than ~1 s (**Fig. 3C**), as is expected from **Eq. 6**. The torque AD is identical for all employed trap stiffnesses for times between 1 and 100 s, and already reaches a torque precision of ~5 pN·nm after 1 s, again much faster than in the MTT (~50 s, **Fig. 2C**) due to the smaller beads used here. The torque precision reaches ~0.5 pN·nm for 100 s measurements (**Fig. 3C**). The angle ADs are well described by the analytical expression in **Eq. 3**, yielding fitted drag coefficients γ_θ (**Fig. 3D**) that are independent of the magnetic field, as expected, and fitted trap stiffnesses κ_θ (**Fig. 3E**) that increase monotonically with the magnetic field. In the field range used in our implementation of the eMTT (1–16 mT), the dependence of κ_θ on field can be reasonably approximated as linear (35) (**Fig. 3E**, dashed black line).

In these eMTT measurements, we start to see deviations from the thermal limit behavior ($\propto \tau^{-1/2}$) after ~100 s, and the torque AD signals for different field strengths begin to differ. In general, for times longer than ~100 s, the torque AD is higher for higher field strengths, due to pronounced drifts apparent as increases in the torque AD with time for long times (**Fig. 3C**, see traces at 4 and 8 mT). The drifts are very likely due to heating of the coils when running relatively high currents to achieve high fields for extended periods of time. Our present implementation of the eMTT requires ~16 A to achieve ~16 mT field and is air-cooled only (35). The heating is most dramatically visible in the trace at 16 mT, which had to be terminated after ~280 s (**Supplementary Fig. S3A**) as the coils reached a temperature of 60 °C, at which point they are shut down by an automatic safety switch. A clear recommendation that emerges from the AD analysis is, therefore, to run at low field strengths and thus trap stiffnesses in the eMTT for optimal torque measurements: in the absence of drift, higher trap stiffnesses do not confer any disadvantages in the torque precision; yet the high currents required for high trap stiffnesses tend to cause significant drifts due to heating and thus deterioration of the torque precision for times longer than ~100 s. In contrast, for low currents and trap stiffnesses, we observe very low levels of drifts even for (very) long measurements, and reach, e.g., a best precision of ~0.1 pN·nm for ~1000 s measurements at $\leq$ 2 mT.

Angle and torque precision in eMTT for different bead sizes. In addition, in the eMTT experiments we probe the effect of different drag coefficients by comparing different bead sizes at roughly constant trap stiffness (**Supplementary Fig. S6**). Similar to the simulations (**Fig. 1C,D**), a higher drag coefficient shifts the AD curve to longer time scales. At intermediate averaging times τ ~10–100 s, the smaller the bead, the better the angle and torque precision, as expected from the corresponding thermal limits (**Eqs. 5**, **6**, respectively). The rotational drag coefficients obtained from the AV fits (**Fig. 3F**, red circles) are in good agreement with predictions of the model (**Fig. 3F**, black squares) that take into account the bead and tether geometry and surface effects (**Eq. S10**), and roughly follow a $\gamma_\theta \sim d^3$ scaling, where d is bead diameter (**Fig. 3F**, solid blue line). The bead size analysis confirms that a decrease in drag coefficient improves the precision in both angle and torque.

As an independent test of the torque precision achieved in the eMTT, we analyzed a high-precision DNA torque measurement that employed 1 μm diameter beads and a measurement time of 200 s per measurement point (**Supplementary Fig. S7A**). The torque AD analysis (**Supplementary Fig. S4F**) suggests that this measurement should achieve a torque precision of ~0.5–0.9 pN·nm at ~200 s. We analyzed the deviations of the measured torque values from a strictly linear behavior in the elastic response regime (**Supplementary Fig. S7B**) and the deviations from constant torque in the DNA melting regime (**Supplementary Fig. S7C**). The deviations are approximately Gaussian distributed with a standard deviation of 0.9 and 0.6 pN·nm for the two regimes respectively, in excellent overall agreement with the expected precision from the AD analysis.

Angle and torque measurements in the OTW. In the optical tweezers measurements, we keep the linear polarization of the trapping beam fixed and measure the torque transferred from the laser beam to a trapped, birefringent cylinder undergoing thermal fluctuations (**Materials and Methods, Fig. 4A**). The cylinders are fabricated out of rutile TiO_2, selected over other materials (e.g. quartz SiO_2) for its extraordinarily high birefringence. While the OTW directly measures angular momentum transfer, and thus torque, the torque traces are recorded in voltage. The corresponding AD can be converted to either the angle AD in degrees (**Fig. 4B**) or the torque AD in pN·nm (**Fig. 4C**) using parameters obtained through a separate calibration process (22). We also fit the torque AD (**Eq. 3**, multiplied by κ_θ^2) to obtain values for the parameters κ_θ and γ_θ. The drag coefficient γ_θ is nearly independent of laser power (**Fig. 4D**) and averages to 0.13 ± 0.01 pN·nm·s, in good agreement with a theoretical value of ~0.12 pN·nm·s (56). The angular trap stiffness κ_θ increases linearly with the laser power (**Fig. 4E**), i.e. quadratically with the electric field amplitude (9). The Allan deviations for the OTW data (**Fig. 4B**,**C**) report on the precision of this experimental apparatus. As in the eMTT, we observe that angular precision improves (e.g. from ~0.03° to ~0.007° at ~10 s (**Fig. 4B**) with increased stiffness (achieved by increasing laser power from 10 to 40 mW). At the highest laser power, the measurements reach an angular precision of ~1° after only 0.3 ms; a much shorter timescale than in the magnetic tweezers measurements that results from the order(s)-of-magnitude higher trap stiffness and lower drag coefficient in the optical tweezers (compare panels **D**, **E** in **Figs. 2-4**). For the torque AD (**Fig. 4C**), all curves

converge to the thermal limit. Similar dependencies for laser powers up to 80 mW were observed in a separate data set (**Supplementary Fig. S9**).

The best torque precision in the OTW achieved is ~0.3 pN·nm, comparable to ~0.1 pN·nm precision achieved in the eMTT measurements. This requires the optimized environmental conditions reflected in **Fig. 4** and **Supplementary Fig. S8** (see, for comparison, **Supplementary Fig. S9** where air currents induced earlier onset of drift) and is achieved after an averaging time of ~10 s at a laser power of 10 mW (**Fig. 4C**). On longer timescales, we find that drift in the OTW becomes dominant and deteriorates the precision. Similar dominance of drift only appears after ~100 s in the eMTT at high Helmholtz fields ($\geq$ 4 mT). The earlier onset of drift in the OTW compared to the eMTT derives from the increased number of optical and electronic components present, coupled to laser power-dependent heating (observable from ~10 s onwards in **Fig. 4B,C**). These clear differences observed in the noise highlight the ability of our AD analysis to detect and compare noise components among different setups and environmental conditions.

Discussion

Examination of the AD provides insights into the achievable precision and optimal measurement duration and parameters. For a hypothetical measurement without drift, the AD can become arbitrarily small, provided the trace is averaged long enough, as the AD decreases in the thermal limit as $\tau^{-1/2}$. This would imply that the precision achievable experimentally could be arbitrarily high. In practice, of course, noise other than the white noise deriving from thermal fluctuations will kick in and limit further improvements in precision. Given the additive nature of the AD (**Eq. 2**), at a certain averaging time τ, drift will start to dominate over the thermal limit; on longer timescales, the precision will no longer improve with averaging, but rather worsen. The resulting minimum in the AD then designates the best achievable precision and hence the optimum measurement time. Different sources of drift will exhibit distinct signatures in the AD. For example, for linear drift, the AD should increase as τ^1 (**Supplementary Text S6**), as we observe for the OTW traces (**Fig. 4B,C**, τ = 10–100 s). If the dominant source of noise has a $1/f$ character, then the AD scales as τ^0 (i.e. becomes constant; **Supplementary Text S6**), as we observe around 2 s in the AD plots for the OTW dataset presented in **Supplementary Fig. S9E,F**.

In this work, we have introduced the use of the AD to evaluate the performance of several instruments designed to measure torque on individual (biological) molecules. In both of the magnetic tweezers measurements, drift does not appear to significantly limit the measurements, even for very long measurement times (**Fig. 3B,C**, τ = 100–1000 s), provided that low enough Helmholtz fields ($\leq$ 2 mT) are used to avoid drifts through heating of the coils in the eMTT configuration. It might be possible to avoid this limitation in future implementations, e.g. by configuring water-cooled coils. Nonetheless, even the current instrument enables measurements with a torque precision better than 1 pN·nm (**Fig. 3C** and **Supplementary Figs. S3F-S5F, S7**). We achieved a similar torque precision (0.3 pN·nm in 10 s, **Fig. 4C;** for direct comparison with the eMTT, see **Supplementary Fig. S10**) in the OTW under the best conditions (low laser power and blocking of air current). Potentially, the precision of the OTW can be enhanced by further improvements to the instrument's long-term stability.

A general lesson from our analysis is that to optimize torque and/or angle precision the drag coefficient should be minimized, in particular by using smaller particles (8). The eMTT data sets clearly demonstrate the improvements in precision obtained through using smaller beads; recent approaches to angle and torque measurements using gold nanoparticles push this development even further (15). Furthermore, once a particle size has been selected, it is generally advisable to maximize the trap stiffness for improved angle (but not torque) precision given measurement times in which precision is thermally limited. However, there are important caveats to this general advice: first, smaller particles usually result in reduced stiffness and achievable torque, because they contain less volume for torque exchange (lower magnetic content in magnetic beads and a shorter light path in birefringent particles); second, increasing the trap stiffness can result in increased drift due to the practical limitations (e.g., heating from increased current in eMTT or laser power in OTW), deteriorating the precision for longer measurement timescales; third, the use of ever smaller particles may push the limits of the detection systems (e.g., pixel size for camera- and diode sensitivity for photodiode-based signal acquisition); fourth, maximization of the trap stiffness and minimization of the drag coefficient reduce the characteristic time τ_c, which demands for faster acquisition systems, as most calibration methods (and particularly AD analysis, see **Supplementary Text S1**), require measurements on timescales shorter than τ_c; and finally, the timescale of

dynamics in the system under investigation and the quantity of interest, angle or torque, ultimately determine the optimal drag coefficient and stiffness of operation.

The AD provides a direct and quantitative measure for the precision in single-molecule experiments. It can therefore be employed as a tool for optimizing experimental assays: it can be used to systematically track down sources of drift and other forms of noise and to determine the optimal measurement time at the desired precision. We foresee that usage of the AD analysis will instruct researchers about the optimal measurement strategy, and thus will facilitate new breakthroughs in the field of single-molecule torque spectroscopy.

Supporting Materials

Supplementary text and figures are available at (*URL will be added here*).

Author Contributions

M.M.v.O., J.L., and N.H.D. designed the research. J.L. and N.H.D. directed the research. T.J. and M.L. performed the MTT and eMTT experiments, respectively. M.M.v.O. and S.H. conducted the OTW experiments. M.M.v.O., S.H., and J.L. analyzed the data. All authors discussed the data and M.M.v.O., S.H., J.L., and N.H.D. wrote the manuscript.

Acknowledgments

We thank Fabian Czerwinski for suggesting the use of AD for the analysis of torque spectroscopy experiments; Richard Janissen, Roland Kieffer, Margreet Docter, Jacob Kerssemakers, Sacha Khaiboulov, Dimitri de Roos, and Belen Solano Hermosilla for technical suggestions; Xander Janssen and Renier Daudey for performing preliminary eMTT measurements; and Roland Dries for assistance with the OTW setup. This work is supported by funding provided by NanoNextNL, a micro- and nanotechnology consortium of the Government of the Netherlands and 130 partners (to N.H.D.); the Foundation for Fundamental Research on Matter (to N.H.D.); the Netherlands Organisation for Scientific Research (to N.H.D. and J.L.); the European Community's Seventh Framework Programme FP7/2007–2013 under grant agreement number 241548 (MitoSys; to N.H.D.); the European Research Council Consolidator grant (DynGenome) under grant number

312221 (to N.H.D.); and the German Research Foundation under grant number SFB 863 (to J.L.).

Supporting Citations

References (57-61) appear in the Supporting Materials.

References

1. Bustamante, C., Z. Bryant, and S. B. Smith. 2003. Ten years of tension: single-molecule DNA mechanics. *Nature.* 421:423-427.
2. Strick, T. R., M. N. Dessinges, G. Charvin, N. H. Dekker, J. F. Allemand, D. Bensimon, and V. Croquette. 2003. Stretching of macromolecules and proteins. *Rep. Prog. Phys.* 66:1-45.
3. Neuman, K. C., and A. Nagy. 2008. Single-molecule force spectroscopy: optical tweezers, magnetic tweezers and atomic force microscopy. *Nat. Methods.* 5:491-505.
4. Puchner, E. M., and H. E. Gaub. 2009. Force and function: probing proteins with AFM-based force spectroscopy. *Curr. Opin. Struct. Biol.* 19:605-614.
5. Vilfan, I. D., J. Lipfert, D. A. Koster, S. G. Lemay, and N. H. Dekker. 2009. Magnetic tweezers for single-molecule experiments. *In* Handbook of Single-Molecule Biophysics. P. Hinterdorfer and A. van Oijen, editors. Springer, pp. 371-395.
6. Dulin, D., J. Lipfert, M. C. Moolman, and N. H. Dekker. 2013. Studying genomic processes at the single-molecule level: introducing the tools and applications. *Nat. Rev. Genet.* 14:9-22.
7. Robinson, A., and A. M. van Oijen. 2013. Bacterial replication, transcription and translation: mechanistic insights from single-molecule biochemical studies. *Nat. Rev. Microbiol.* 11:303-315.
8. Bryant, Z., F. C. Oberstrass, and A. Basu. 2012. Recent developments in single-molecule DNA mechanics. *Curr. Opin. Struct. Biol.* 22:304-312.
9. Lipfert, J., M. M. van Oene, M. Lee, F. Pedaci, and N. H. Dekker. 2015. Torque spectroscopy for the study of rotary motion in biological systems. *Chem. Rev.* 115:1449-1474.
10. Bryant, Z., M. D. Stone, J. Gore, S. B. Smith, N. R. Cozzarelli, and C. Bustamante. 2003. Structural transitions and elasticity from torque measurements on DNA. *Nature.* 424:338-341.
11. Gore, J., Z. Bryant, M. D. Stone, M. Nollmann, N. R. Cozzarelli, and C. Bustamante. 2006. Mechanochemical analysis of DNA gyrase using rotor bead tracking. *Nature.* 439:100-104.
12. Gore, J., Z. Bryant, M. Nollmann, M. U. Le, N. R. Cozzarelli, and C. Bustamante. 2006. DNA overwinds when stretched. *Nature.* 442:836-839.
13. Oberstrass, F. C., L. E. Fernandes, and Z. Bryant. 2012. Torque measurements reveal sequence-specific cooperative transitions in supercoiled DNA. *Proc. Natl. Acad. Sci. U.S.A.* 109:6106-6111.
14. Oberstrass, F. C., L. E. Fernandes, P. Lebel, and Z. Bryant. 2013. Torque spectroscopy of DNA: base-pair stability, boundary effects, backbending, and breathing dynamics. *Phys. Rev. Lett.* 110:178103.

15. Lebel, P., A. Basu, F. C. Oberstrass, E. M. Tretter, and Z. Bryant. 2014. Gold rotor bead tracking for high-speed measurements of DNA twist, torque and extension. *Nat. Methods.* 11:456-462.
16. Friese, M. E. J., T. A. Nieminen, N. R. Heckenberg, and H. Rubinsztein-Dunlop. 1998. Optical alignment and spinning of laser-trapped microscopic particles. *Nature.* 394:348-350.
17. Oroszi, L., P. Galajda, H. Kirei, S. Bottka, and P. Ormos. 2006. Direct measurement of torque in an optical trap and its application to double-strand DNA. *Phys. Rev. Lett.* 97:058301.
18. La Porta, A., and M. D. Wang. 2004. Optical torque wrench: angular trapping, rotation, and torque detection of quartz microparticles. *Phys. Rev. Lett.* 92:190801.
19. Forth, S., C. Deufel, M. Y. Sheinin, B. Daniels, J. P. Sethna, and M. D. Wang. 2008. Abrupt buckling transition observed during the plectoneme formation of individual DNA molecules. *Phys. Rev. Lett.* 100:148301.
20. Inman, J., S. Forth, and M. D. Wang. 2010. Passive torque wrench and angular position detection using a single-beam optical trap. *Opt. Lett.* 35:2949-2951.
21. Pedaci, F., Z. X. Huang, M. van Oene, S. Barland, and N. H. Dekker. 2011. Excitable particles in an optical torque wrench. *Nat. Phys.* 7:259-264.
22. Pedaci, F., Z. Huang, M. van Oene, and N. H. Dekker. 2012. Calibration of the optical torque wrench. *Opt. Express.* 20:3787-3802.
23. Deufel, C., S. Forth, C. R. Simmons, S. Dejgosha, and M. D. Wang. 2007. Nanofabricated quartz cylinders for angular trapping: DNA supercoiling torque detection. *Nat. Methods.* 4:223-225.
24. Gutiérrez-Medina, B., J. O. Andreasson, W. J. Greenleaf, A. La Porta, and S. M. Block. 2010. An optical apparatus for rotation and trapping. *Meth. Enzymol.* 475:377-404.
25. Huang, Z., F. Pedaci, M. van Oene, M. J. Wiggin, and N. H. Dekker. 2011. Electron beam fabrication of birefringent microcylinders. *ACS Nano.* 5:1418-1427.
26. Ha, S., R. Janissen, Y. Y. Ussembayev, M. M. van Oene, B. Solano, and N. H. Dekker. 2016. Tunable top-down fabrication and functional surface coating of single-crystal titanium dioxide nanostructures and nanoparticles. *Nanoscale.* 8:10739-10748.
27. Parkin, S. J., R. Vogel, M. Persson, M. Funk, V. L. Y. Loke, T. A. Nieminen, N. R. Heckenberg, and H. Rubinsztein-Dunlop. 2009. Highly birefringent vaterite microspheres: production, characterization and applications for optical micromanipulation. *Opt. Express.* 17:21944-21955.
28. Ramaiya, A., B. Roy, M. Bugiel, and E. Schäffer. 2017. Kinesin rotates unidirectionally and generates torque while walking on microtubules. *Proc. Natl. Acad. Sci. U.S.A.* 114:10894.
29. Mosconi, F., J. F. Allemand, and V. Croquette. 2011. Soft magnetic tweezers: a proof of principle. *Rev. Sci. Instrum.* 82:034302.
30. Celedon, A., I. M. Nodelman, B. Wildt, R. Dewan, P. Searson, D. Wirtz, G. D. Bowman, and S. X. Sun. 2009. Magnetic tweezers measurement of single molecule torque. *Nano Lett.* 9:1720-1725.
31. Kauert, D. J., T. Kurth, T. Liedl, and R. Seidel. 2011. Direct mechanical measurements reveal the material properties of three-dimensional DNA origami. *Nano Lett.* 11:5558-5563.
32. Lipfert, J., J. W. J. Kerssemakers, T. Jager, and N. H. Dekker. 2010. Magnetic torque tweezers: measuring torsional stiffness in DNA and RecA-DNA filaments. *Nat. Methods.* 7:977-980.

33. Lipfert, J., M. Wiggin, J. W. Kerssemakers, F. Pedaci, and N. H. Dekker. 2011. Freely orbiting magnetic tweezers to directly monitor changes in the twist of nucleic acids. *Nat. Commun.* 2:439.
34. Lipfert, J., M. Wiggin, J. W. Kerssemakers, F. Pedaci, and N. H. Dekker. 2015. Corrigendum: Freely orbiting magnetic tweezers to directly monitor changes in the twist of nucleic acids. *Nat. Commun.* 6:7192.
35. Janssen, X. J., J. Lipfert, T. Jager, R. Daudey, J. Beekman, and N. H. Dekker. 2012. Electromagnetic torque tweezers: a versatile approach for measurement of single-molecule twist and torque. *Nano Lett.* 12:3634-3639.
36. Moffitt, J. R., Y. R. Chemla, S. B. Smith, and C. Bustamante. 2008. Recent advances in optical tweezers. *Annu. Rev. Biochem.* 77:205-228.
37. Capitanio, M., and F. S. Pavone. 2013. Interrogating biology with force: single molecule high-resolution measurements with optical tweezers. *Biophys. J.* 105:1293-1303.
38. Perkins, T. T. 2014. Ångström-precision optical traps and applications. *Annu. Rev. Biophys.* 43:279-302.
39. Andersson, M., F. Czerwinski, and L. B. Oddershede. 2011. Optimizing active and passive calibration of optical tweezers. *J. Opt.* 13:044020.
40. Huhle, A., D. Klaue, H. Brutzer, P. Daldrop, S. Joo, O. Otto, U. F. Keyser, and R. Seidel. 2015. Camera-based three-dimensional real-time particle tracking at kHz rates and Ångström accuracy. *Nat. Commun.* 6:5885.
41. Dulin, D., T. J. Cui, J. Cnossen, M. W. Docter, J. Lipfert, and N. H. Dekker. 2015. High spatiotemporal-resolution magnetic tweezers: calibration and applications for DNA dynamics. *Biophys. J.* 109:2113-2125.
42. Gibson, G. M., J. Leach, S. Keen, A. J. Wright, and M. J. Padgett. 2008. Measuring the accuracy of particle position and force in optical tweezers using high-speed video microscopy. *Opt. Express.* 16:14561-14570.
43. Czerwinski, F., A. C. Richardson, and L. B. Oddershede. 2009. Quantifying noise in optical tweezers by Allan variance. *Opt. Express.* 17:13255-13269.
44. Mahamdeh, M., and E. Schäffer. 2009. Optical tweezers with millikelvin precision of temperature-controlled objectives and base-pair resolution. *Opt. Express.* 17:17190-17199.
45. Allan, D. W. 1966. Statistics of atomic frequency standards. *Proc. IEEE.* 54:221-230.
46. Allan, D. W., M. A. Weiss, and J. L. Jespersen. 1991. A frequency-domain view of time-domain characterization of clocks and time and frequency distribution systems. *In* Proceedings of the 45th Annual Symposium on Frequency Control (IEEE), pp. 667-678.
47. Lansdorp, B. M., and O. A. Saleh. 2012. Power spectrum and Allan variance methods for calibrating single-molecule video-tracking instruments. *Rev. Sci. Instrum.* 83:025115.
48. Lansdorp, B. M., and O. A. Saleh. 2014. Erratum: "Power spectrum and Allan variance methods for calibrating single-molecule video-tracking instruments" [Rev. Sci. Instrum. 83, 025115 (2012)]. *Rev. Sci. Instrum.* 85:019901.
49. Czerwinski, F. 2010. Allan v3.0. *In* Matlab Central File Exchange. http://mathworks.com/matlabcentral/fileexchange/26659-allan-v3-0
50. van Oene, M. M., L. E. Dickinson, F. Pedaci, M. Kober, D. Dulin, J. Lipfert, and N. H. Dekker. 2015. Biological magnetometry: torque on superparamagnetic beads in magnetic fields. *Phys. Rev. Lett.* 114:218301.

51. Lipfert, J., J. W. J. Kerssemakers, M. Rojer, and N. H. Dekker. 2011. A method to track rotational motion for use in single-molecule biophysics. *Rev. Sci. Instrum.* 82:103707.
52. Strick, T. R., V. Croquette, and D. Bensimon. 1998. Homologous pairing in stretched supercoiled DNA. *Proc. Natl. Acad. Sci. U.S.A.* 95:10579-10583.
53. Leach, J., H. Mushfique, S. Keen, R. Di Leonardo, G. Ruocco, J. M. Cooper, and M. J. Padgett. 2009. Comparison of Faxen's correction for a microsphere translating or rotating near a surface. *Phys. Rev. E.* 79:026301.
54. Faxen, H. 1922. Der Widerstand gegen die Bewegung einer starren Kugel in einer zähen Flüssigkeit, die zwischen zwei parallelen ebenen Wänden eingeschlossen ist. *Ann. Phys.* 68:89-119.
55. Lobo, S., C. Escauriaza, and A. Celedon. 2011. Measurement of surface effects on the rotational diffusion of a colloidal particle. *Langmuir.* 27:2142-2145.
56. Ortega, A., and J. García de la Torre. 2003. Hydrodynamic properties of rodlike and disklike particles in dilute solution. *J. Chem. Phys.* 119:9914-9919.
57. Howe, D. A., D. W. Allan, and J. A. Barnes. 1981. Properties of signal sources and measurement methods. *In* Proceedings of the 35th Annual Symposium on Frequency Control (IEEE), pp. A1-A47.
58. Volpe, G., S. Gigan, and G. Volpe. 2013. Simulation of a Brownian particle in an optical trap. *Am. J. Phys.* 81:224-230.
59. Rutman, J. 1978. Characterization of phase and frequency instabilities in precision frequency sources: fifteen years of progress. *Proc. IEEE.* 66:1048-1075.
60. Wong, W. P., and K. Halvorsen. 2006. The effect of integration time on fluctuation measurements: calibrating an optical trap in the presence of motion blur. *Opt. Express.* 14:12517-12531.
61. Yasuda, R., H. Miyata, and K. Kinosita, Jr. 1996. Direct measurement of the torsional rigidity of single actin filaments. *J. Mol. Biol.* 263:227–236.

FIGURE CAPTIONS

Figure 1. Allan deviation of simulated traces. A) Illustration of the octave-sampled overlapping Allan deviation. The example trace (black) contains 16 data points. Each data point is recorded during the sampling period τ_s. The data are split into bins of m data points. In octave-sampled data, $m = 2^{\text{integer}}$ (going from red to yellow, m = 1, 2, 4, 8). Splitting in bins is possible in m different frame shifts. For m = 8, only three frame shifts are displayed for clarity. **B)** Simulated angular traces ≈ 1700 s each sampled at 50 kHz (corresponding to 8.5×10^7 data points), for rotational Brownian motion of particles in harmonic traps. The left panel shows a zoom-in on the first 50 s of the traces, and the right panel shows the histograms for the full traces. The traces are offset vertically for clarity. The red, green, and blue traces are simulations with drag coefficient γ_θ = 100, 10, and 10 pN·nm·s, and trap stiffness κ_θ = 1000, 1000, and 100 pN·nm/rad, respectively. **C,D)** Angle and torque Allan deviation (AD) for the traces in **B)**. Colored lines (circles) reflect the normal AD and octave-sampled overlapping AD, respectively. The results of the fits are indicated by solid black lines and their extrapolations as dashed black lines (**Eq. 3**). The fitted parameters are γ_θ = 99.4 ± 0.1, 9.9 ± 0.01, and 10.0 ± 0.01 pN·nm·s and κ_θ = 1009.6 ± 36.6, 998.9 ± 9.7, and 99.6 ± 2.9 pN·nm/rad for the red, green, and blue data, respectively, from N = 5 independent simulated traces for each condition. The dash-dotted and dashed magenta lines are the diffusion and thermal limits, shown for the green datasets only.

Figure 2. Angle and torque precision in the magnetic torque tweezers (MTT). A) Schematic of the "classical" MTT implementation (32). Angle tracking is achieved by attaching a smaller (1 μm diameter) non-magnetic marker bead (green) to a larger (2.8 μm diameter) magnetic bead (brown) and tracking the rotation of the bead pair from CCD images (inset). The magnetic bead is tethered to a glass slide (blue) by a single DNA molecule (black), held and manipulated in a weak rotational trap set up by a vertically aligned permanent magnets with a side magnet added (on top). The axis of bead rotation is indicated by the vertical dashed black line. **B)** Octave-sampled overlapping Allan deviation (AD) of 32 angle traces of 100 s each sampled at 35 Hz (corresponding to 3.5×10^3 data points), recorded in a torque measurement on a single 7.9 kbp DNA molecule (each trace is shown as a distinctly colored solid line, denoting the number of applied turns). The octave-sampled points for a single trace are shown as black circles. The fit of the analytical expression for the AV (**Eq. 3**) is shown as a solid black line and its extrapolation as a dashed black line. The thermal limit is indicated as a dashed magenta line. **C)** Torque AD of the same traces as **B)** obtained by multiplication with the corresponding trap stiffnesses (color-coding is as in **B)**). Similar to **B)**, octave-sampled points for one trace are shown as black circles and the fit to **Eq. 3** is shown as a solid black line, and its extrapolation is shown as a dashed black line. The thermal limit is indicated as a dashed magenta line. **D)** The values for the trap stiffness κ_θ determined from the fits for all traces in **B)**. The data are approximately Gaussian distributed (solid black line) with a standard deviation of ~45 pN·nm/rad. **E)** Rotational friction coefficients γ_θ (distinctly colored circles) determined from the AV fits for all traces in **B)** shown as a function of the height of the bead above the flow cell surface. The color-coding denotes the number of applied turns. The solid black line reflects a prediction for the rotational friction coefficient of a 2.8 μm diameter bead rotating on a circular trajectory, taking into account corrections due to the presence of the surface.

Figure 3. Angle and torque precision in the electromagnetic torque tweezers (eMTT). A) Schematic of the eMTT setup (35). A magnetic bead (brown) is tethered to a glass slide (blue) by a single 3.4 kbp DNA molecule (black). The bead is lifted off from the surface by a cylindrical magnet (on top). Four coils (only two are shown here) generate an in-plane magnetic field to orient the bead. Here, the angular orientation of the magnetic bead is deduced from its spatial position within a circular annulus whose radius is set by the distance between the tether attachment point and the pole of the magnetic bead (35). The axis of bead rotation is indicated by the vertical dashed black line. **B)** Angle Allan deviation (AD) of angle traces ≈ 2600 s each (except at 16 mT; 280 s) sampled at 100 Hz (corresponding to 2.6×10^5 data points), recorded on a single DNA tethered bead at 1, 2, 4, 8, and 16 mT (going from dark brown to light brown). Colored lines (circles) reflect the normal AD and octave-sampled overlapping AD, respectively. The octave-sampled data are used to fit (solid black lines) the data to the analytical expression (**Eq. 3**), and their extrapolations are shown as dashed black lines. The dashed magenta line indicates the thermal limit for the stiffest trap. **C)** Torque AD of the same traces as **B)** obtained by multiplication with the corresponding trap stiffnesses. The color-coding is the same as in **B)**. The dashed magenta line indicates the thermal limit. **D,E)** The values of the rotational drag coefficient γ_θ and the rotational trap stiffness κ_θ obtained from the fits in **B)**. The data points and their corresponding error bars denote the average and standard deviation, respectively, from N = 5 independent measurements. In **D),** the dashed black line is a constant-value fit to the drag coefficients. In **E)**, the dashed black line is a linear fit to the data through the origin. **F)** Drag coefficients from AV fits for three different bead sizes (d = 0.7, 1.05, and 2.8 μm; **Supplementary Figs. S3-S5**). Red circles and error bars are the drag coefficients (mean ± STD) determined from AV fits for differently sized beads (**Supplementary Figs. S3G-S5G**) averaged over measurements at different field strengths. Black squares are the predictions from **Eq. S10**. The solid blue line is a fit of the scaling relation $\gamma_\theta \sim d^3$.

Figure 4. Angle and torque precision in the optical torque wrench (OTW). A) Schematic of the OTW setup (22). The objective lens focuses a linearly polarized laser beam input (red), and traps a birefringent cylinder (gray) near the focus within a flow cell. Manipulation of the linear polarization allows us to control the angular position of the particle. At the output of the trap, the laser light is collected by a condenser lens. The polarization state of the output reports on the torque transferred from beam to particle. The axis of cylinder rotation is indicated by the vertical dashed black line. **B)** Angle Allan deviation (AD) obtained from **C)** by division with the corresponding trap stiffnesses. Colored lines (circles) reflect the normal AD and octave-sampled overlapping AD, respectively. The color-coding is the same as in **C)**. The dashed magenta line indicates the thermal limit for the stiffest trap. **C)** Torque AD of torque traces 200 s each sampled at 100 kHz (corresponding to 2.0×10^7 data points), recorded on a single rutile TiO_2 cylinder at 10, 20, and 40 mW (going from dark blue to light green). The octave-sampled data are used to fit (solid black lines) the data to the analytical expression (**Eq. 3**, multiplied by κ_θ^2), and their extrapolations are shown as dashed black lines. The fits only provide two independent parameters, γ_θ and κ_θ, so the system was precalibrated (22) to obtain the detector sensitivity in units of pN·nm/mV. The dashed magenta line indicates the thermal limit. The dash-dotted black line has slope +1, corresponding to linear drift. **D,E)** The values of the rotational drag coefficient γ_θ and the rotational trap stiffness κ_θ obtained from the fits in **C)**. The data points and their corresponding error bars denote the average and standard deviation, respectively, from N = 5 independent measurements. In **D)**, the

dashed black line is a constant-value fit to the drag coefficients. In **E)**, the dashed black line is a linear fit to the data through the origin.

FIGURES

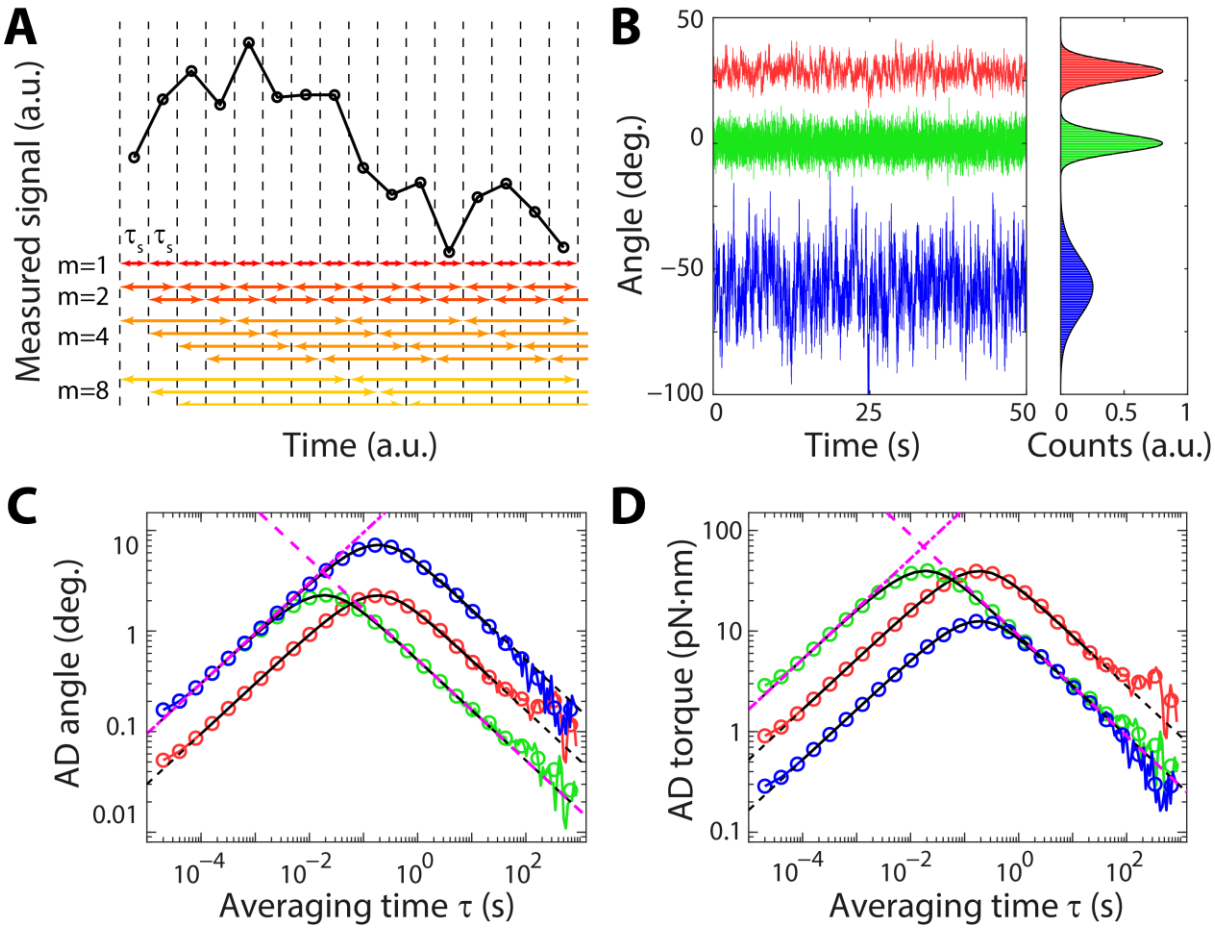

Figure 1. Allan deviation of simulated traces.

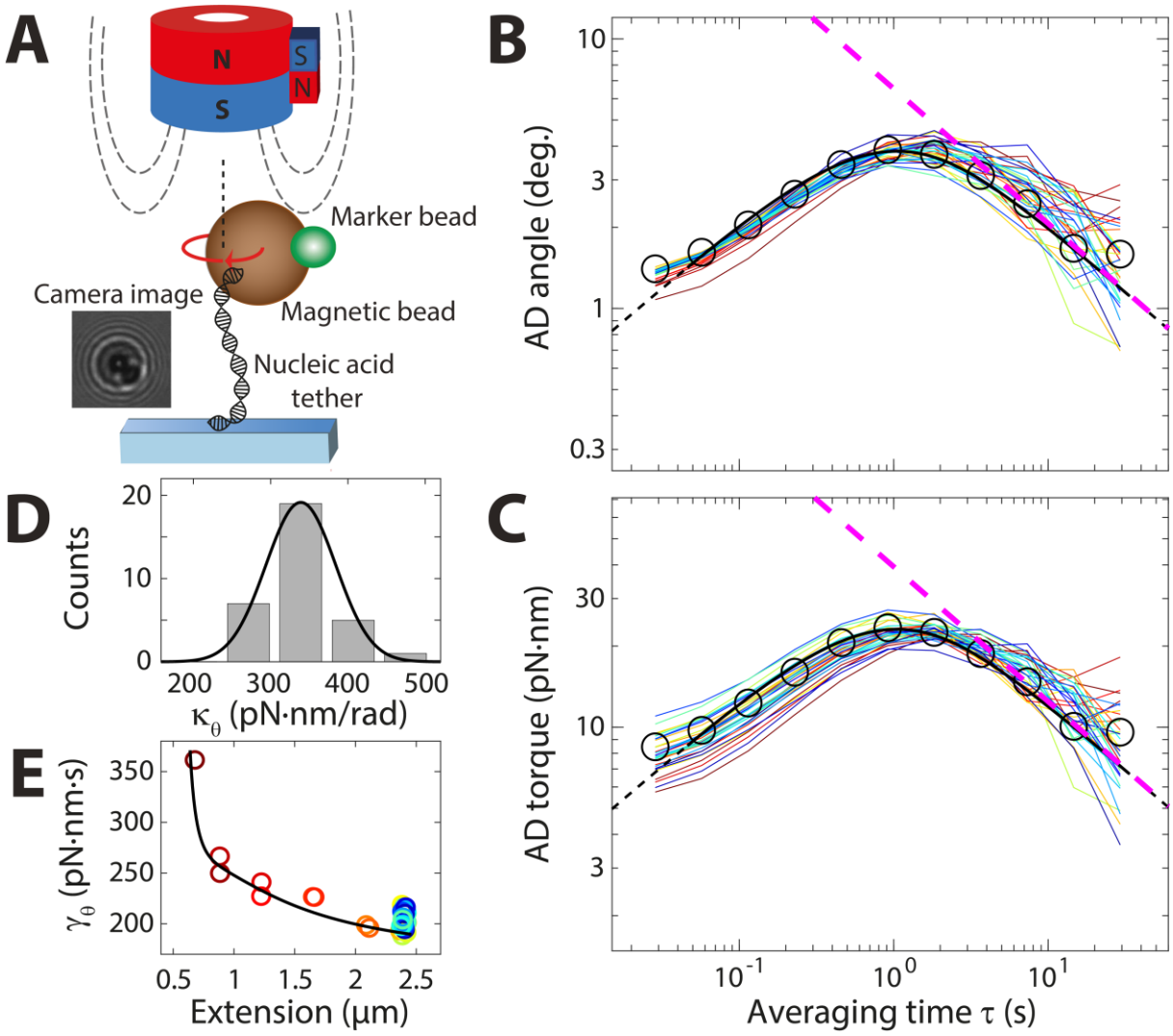

Figure 2. Angle and torque precision in the magnetic torque tweezers (MTT).

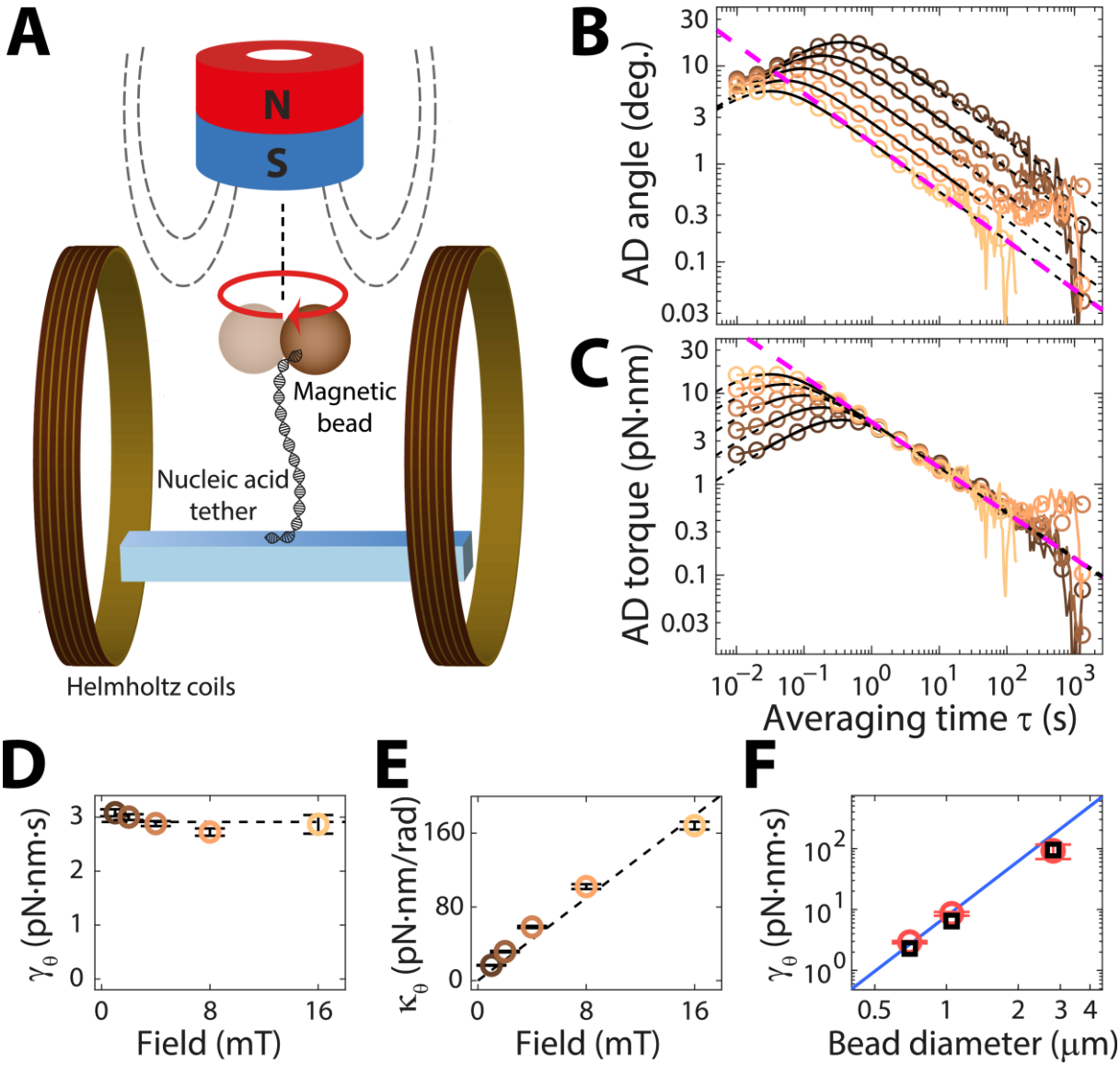

Figure 3. Angle and torque precision in the electromagnetic torque tweezers (eMTT).

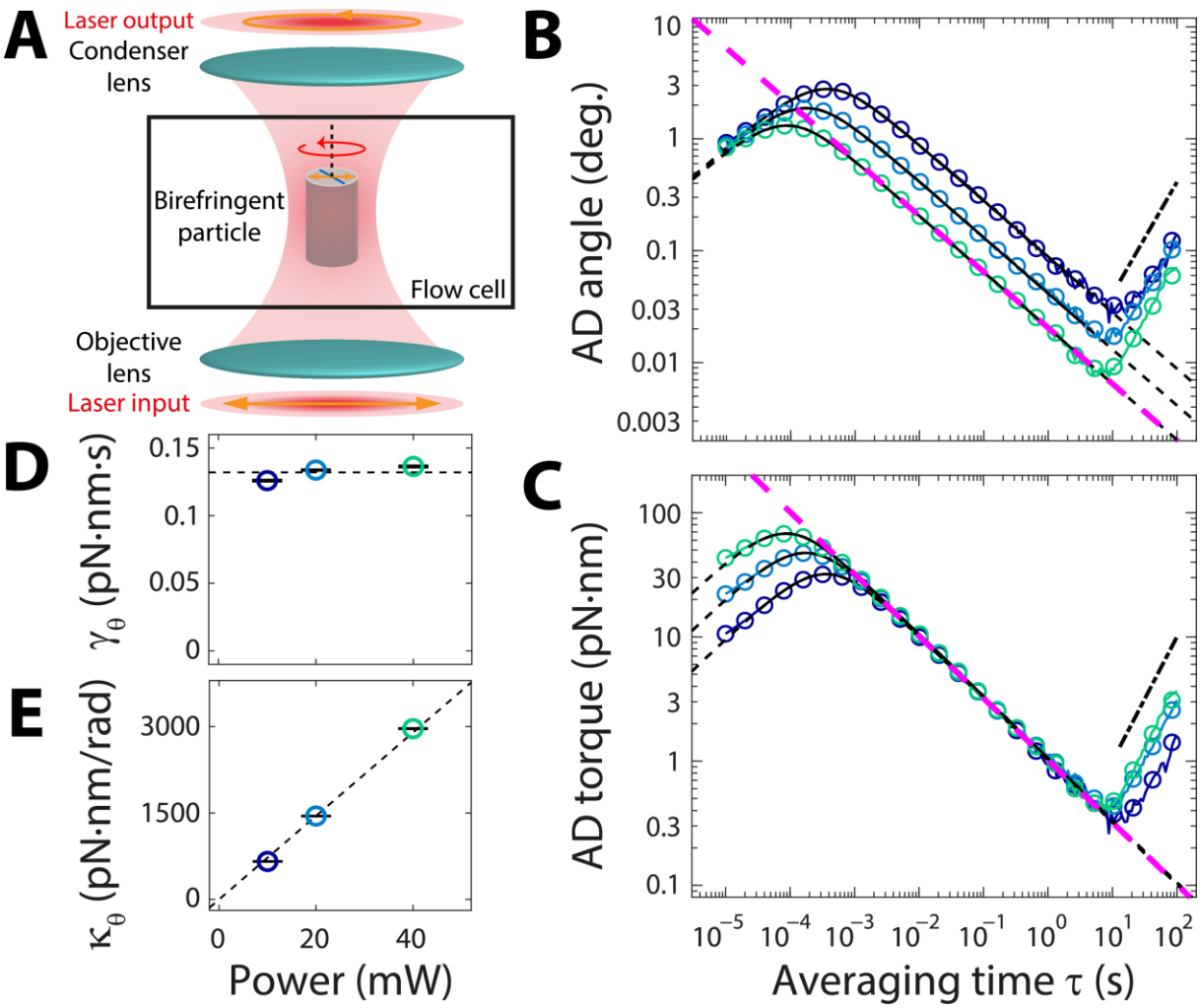

Figure 4. Angle and torque precision in the optical torque wrench (OTW).